





# Full-view volumetric photoacoustic imaging using a hemispheric transducer array combined with an acoustic reflector

MINGLI SUN,<sup>1,†</sup> XUANHAO WANG,<sup>2,†</sup>  YUQI WANG,<sup>2</sup> YUQIAN MENG,<sup>2</sup> DA GAO,<sup>2</sup> CHIYE LI,<sup>2</sup>  RUI MIN CHEN,<sup>2</sup> KAIKAI HUANG,<sup>3</sup> AND JUNHUI SHI<sup>2,\*</sup>

<sup>1</sup>*School of Science, Zhejiang University of Science and Technology, Hangzhou 310023, China*

<sup>2</sup>*Zhejiang Lab, Hangzhou 311100, China*

<sup>3</sup>*School of Physics, Zhejiang University, Hangzhou 310027, China*

<sup>†</sup>These authors contributed equally to this work.

\*[junhuishi@outlook.com](mailto:junhuishi@outlook.com)

**Abstract:** Photoacoustic computed tomography (PACT) has evoked extensive interest for applications in preclinical and clinical research. However, the current systems suffer from the limited view provided by detection setups, thus impeding the sufficient acquisition of intricate tissue structures. Here, we propose an approach to enable fast 3D full-view imaging. A hemispherical ultrasonic transducer array combined with a planar acoustic reflector serves as the ultrasonic detection device in the PACT system. The planar acoustic reflector can create a mirrored virtual transducer array, and the detection view range can be enlarged to cover approximately  $3.7\pi$  steradians in our detection setup. To verify the effectiveness of our proposed configuration, we present the imaging results of a hair phantom, an in vivo zebrafish larva, and a leaf skeleton phantom. Furthermore, the real-time dynamic imaging capacity of this system is demonstrated by observing the movement of zebrafish within 2 s. This strategy holds great potential for both preclinical and clinical research by providing more detailed and comprehensive images of biological tissues.

© 2024 Optica Publishing Group under the terms of the [Optica Open Access Publishing Agreement](#)

## 1. Introduction

Photoacoustic imaging (PAI) relies on the photoacoustic (PA) effect and forms images by detecting ultrasonic waves that result from the thermoelastic expansion following the absorption of pulsed light within biological tissues [1–3]. It combines the high contrast of optical imaging with deep penetration of ultrasound imaging, thereby providing high-resolution imaging capable of visualizing both anatomical and functional details. Photoacoustic computed tomography (PACT), a significant implementation of PAI, employs diffused pulsed light to illuminate the region of interest, and the PA signals are captured by ultrasonic transducers positioned at various angles to reconstruct an image of the target [3–5]. The imaging depth of PACT spans from millimeters to centimeters, while the spatial resolution ranges from tens to hundreds of micrometers [6–9]. PACT has emerged as a preeminent biomedical imaging technique in both preclinical and clinical research, such as breast cancer screening, tumor diagnosis, and brain imaging [10–15].

In PACT, ultrasonic transducer arrays integrating hundreds of individual elements are commonly employed to expedite data acquisition. The linear transducer arrays were predominantly used in early systems [16–21]. However, the narrow receiving angles of these transducers result in PA images lack of the integrity of certain absorptive tissue features. To address the limited-view problem inherent in linear transducer array, various approaches have been proposed. The circular scanning of linear transducer array or rotating the sample can achieve full-view imaging at the cost of time-consuming and mechanical complexity [22,23], which is deficient in speed or stability.

Gateau *et al.* employed a ground glass diffuser and scanned it to generate optical speckles for full-view PA imaging, thereby mitigating the time constraints associated with traditional mechanical scanning methods [24]. However, the motion artifacts were introduced and the imaging depth is limited to superficial structures. W. Shu *et al.* utilized two linear transducer arrays to receive PA signals from different orientations [25]. The positions of two transducer arrays can be adjusted to fit the specific geometry of an imaging site. Other proposed methods, such as bi-directional scanning of two linear transducer arrays and the integration of linear array detectors [26–28], suffer from shallow imaging depth and pronounced anisotropy in spatial resolution. Acoustic reflectors can redirect the undetectable PA waves toward the transducer array, thereby augmenting the effective detection aperture without compromising the imaging speed. Huang *et al.* [29] placed an acoustic reflector at a 45 deg angle relative to the linear transducer array. The reflector forms a virtual array that is perpendicular to the physical array and can double the detection view. Li *et al.* [30,31] tripled the detection view angle by two planar acoustic reflectors set at 120 degrees relative to each other. Ellowood *et al.* [32] extended the effective aperture of a linear transducer array with two acoustic reflectors that are perpendicular to the array surface. However, limited by the inherent linear array structure or the element number, these methods are inadequate in spatial coverage and imaging depth.

Ultrasonic transducer arrays with a large aperture and an increased number of elements can provide higher resolution and more detailed imaging. To date, several array geometries have been developed and utilized in PACT. For example, curved and arc-shaped transducer arrays composed of 64 elements were employed for functional and structural imaging of small animals in vivo [10,33,34]. A semi-cylindrical transducer array with 64 elements was specifically designed for in vivo imaging of human finger [35]. The complete full-ring ultrasonic transducer arrays, comprising 512 elements, were employed for whole-body structural imaging of mice, the visualization of vasculature in human extremities, observing functional connectivity and tracking unlabelled circulating tumor cells in the mouse brain [11, 36–38]. Furthermore, planar, hand-held spherical and concave shapes of transducer arrays were used for human imaging and pathological diagnosis [39–42]. However, a large aperture size may also introduce challenges associated with the ‘finite aperture effect’, such as reduced high-quality imaging region and the potential need for complex reconstruction algorithms to mitigate the associated image degradation [43]. The hemispherical transducer array was firstly designed by Kruger *et al.* and was used to capture the PA images of mouse abdominal section [44,45]. This ultrasonic detector consists of an array of 128 individual transducer elements arranged in a spiral pattern on a hemispherical surface, and the array density could be increased by multi-angle rotation. Hemispherical transducer arrays with 512 elements were developed for the visualization of vasculature and tumor-related blood vessels in human breast [46–48]. Subsequently, hemispherical transducer arrays with 1024 elements were engineered for dynamic whole-body imaging and functional brain imaging of live mouse [49,50]. These systems with thousands of elements can offer substantial imaging depth, relatively uniform spatial resolution, and rapid imaging speed. However, the maximum view angle is limited by approximately  $2\pi$  steradians, and the signals are still lost outside the detection area, which hinders the sufficient acquisition of intricate tissue structures. Recently,  $3.8\pi$  steradians was achieved by rotating and translating a ring-shaped detector array, but this method is deficient in imaging speed, spatial resolution, and system stability [51].

Moreover, the advanced image reconstruction algorithms have been extensively developed for compensating limited view and improving the image quality in recent years, which include deconvolution reconstruction, compressed sensing, iteration reconstruction, sparsity-based reconstruction and deep learning [52–62]. Such approaches typically require high computational complexity or large number of datasets for network training.

In this study, we propose a 3D PACT system that employs a hemispherical ultrasonic transducer array combined with an acoustic reflector placed above it to broaden the detection view. This

system can overcome the limited view challenge of existing systems and achieve fast volumetric imaging without mechanical scanning. The acoustic reflector serves as a virtual transducer array, and the detection view range can be enlarged to cover approximately  $3.7\pi$  steradians in our detection setup. To validate the feasibility and effectiveness of our proposed configuration, the imaging results of a hair phantom, an in vivo zebrafish larva and a leaf skeleton phantom are exhibited. The dynamic imaging capacity of the system is demonstrated by imaging an in vivo zebrafish larva within 2 s. The large field of view, isotropic spatial resolution, and fast imaging speed of our system are advantageous for the improvement of image quality.

## 2. Materials and methods

### 2.1. 3D-PACT system

Our 3D-PACT system comprises several major modules: (i) the illumination apparatus, including a wavelength-tunable pulsed laser, and an optical fiber bundle; (ii) the ultrasound detection array; (iii) the planar acoustic reflector with translation and rotation; (iv) the parallel data acquisition modules. Figure 1(a) displays the schematic diagram of the system setup. An Nd: YAG laser (Nimma-900, 10 Hz repetition rate, pulse duration < 10 ns, Beamtech Optronics Co., Ltd) equipped with optical parametric oscillator (OPO) module (Continuum-OPO, Deyang Tech Co., Ltd) is used as an excitation source. By deflecting the mirror of the built-in optical path, a pumped laser of 532 nm and a tunable spectral range of 650 nm to 900 nm can be achieved, respectively. To reduce the inhomogeneity caused by the attenuation and scattering of light as it travels through the tissue, we adopt a dual illumination mode, which simultaneously illuminates the object from both above and below. The object is placed in the chamber center. The output OPO laser beam is divided into two equal-energy paths through a beam splitter (GCC-411113, Daheng New Epoch Technology Inc.). The reflected portion passes through an engineered diffuser (EDC-10-G-1R, RPC Photonics Inc.) that is sealed in a hole at the bottom of the hemispherical shell. This diffuser enables laser to illuminate the object evenly from below. The other transmitted portion is guided through an optical fiber bundle and vertically illuminates the object from above the detection chamber. Figure 1(b) is the structure diagram of the hemispherical ultrasonic transducer array. The detection array consists of 1024 elements integrated within a hemispherical shell, with a curvature radius of 100 mm (3.5C3.5-SR100-1024, ULISO TECH Co., Ltd). Each element in the array is designed with a central frequency of 3.5 MHz, a diameter of 3.5 mm, and a bandwidth of 72%. These elements are evenly distributed on the inner surface of the hemispherical shell following the Fibonacci grid, and any two adjacent elements are spaced 5.4 mm apart. Integrated operational amplifier chips (PSA4-5043+, Mini-Circuits) are adopted for the lab-made preamplifier boards to amplify the weak PA signals and enhance the signal-to-noise ratio (SNR). The data acquisition (DAQ) system is composed of four DAQ parallel modules (40 MHz sampling rate, 9~48 dB programmable gain, 12.5 kHz to 25 MHz analog bandwidth, Legion ADC, Photosound), and each DAQ module is equipped with 256-channel analog-to-digital converters (ADCs), featuring an adjustable gain range of 12 to 51 dB. The DAQ boards and preamplifier boards are encapsulated into a metal box, which is grounded to realize electromagnetic compatibility. The box is mounted directly onto the interface of the transducer array to reduce coupling noise. A digital delay generator (DG645, Stanford Research Systems) is used to synchronize the triggering of the laser and the acquisition modules of the DAQ system.

A customized BK7 optical glass with a diameter of 80 mm and thickness of 10 mm, serving as an acoustic reflector, is connected to an adjustable frame and positioned horizontally near the detector center. The imaging object is meticulously crafted within an agarose gel, and is closely adhered to below the acoustic reflector, ensuring a bubble-free state. During the imaging process, the sample is immersed in the hemispherical chamber filled with deionized water. Figure 1(c) presents the schematic for the placement of the imaging object, and the corresponding physical configuration shown in Supplement 1, Fig. S1. The optical energy reaching the sample surface

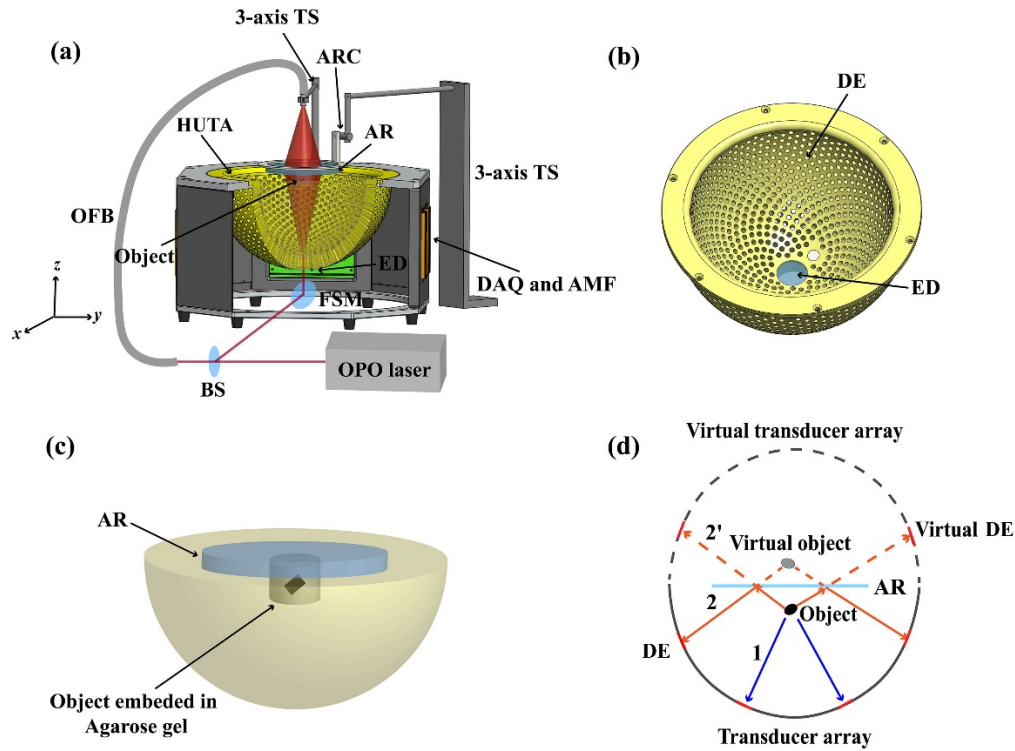


**Fig. 1.** The 3D-PACT system based on the hemispheric ultrasonic transducer array with an acoustic reflector. (a) Schematic diagram of experimental setup. (b) Structure diagram of the hemispheric ultrasonic transducer array. (c) Diagram of the placement of imaging object. (d) Diagram of the propagation and detection of ultrasound waves. HUTA, hemispherical ultrasonic transducer array; OFB, optical fiber bundle; BS, beam splitter; FSM, front-silvered mirror; ED, engineered diffuser; DAQ, data acquisition module; AMF, preamplifier board; TS, translation stage; AR, acoustic reflector; ARC, adjustable rod clamp; DE, detector elements.

meets the criterion of the American National Standards Institute (ANSI) safety limit. As depicted in Fig. 1(d), the laser-induced PA waves from beneath the object can be directly detected by the detector elements (DE) of the physical array, depicted as the solid blue of path 1. PA waves from the upper portion of the object are initially reflected by the acoustic reflector and then captured by the DE, as illustrated by the solid orange line of path 2. These waves can also be conceptualized as being detected by the virtual DE of a virtual array situated in an acoustic homogeneous medium, as indicated by the dashed orange line of path 2'. This system is functionally composed of two hemispheric transducer arrays that are symmetrically positioned around the acoustic reflector. The detection view range approximately  $3.7\pi$  steradians can be achieved in our detection setup (see Supplement 1, Fig. S1). It should be noted that, if the radius of the acoustic reflector is large enough, such as 100 mm, the detection view range can cover  $4\pi$  steradians and a completely enclosed space for the object will be achieved. All the experiment procedures were conducted in conformity with the National Institutes of Health Guidelines on the Care and Use of Laboratory Animal of Beijing Vital River Laboratory Animal Technology Co., Ltd.

## 2.2. Object preparation

For the preparation of hair phantom, as depicted in Fig. 2(a), two cross-tilted human hairs were first embedded in a cylindrical block of solid agarose gel, and several drops of melted agar were applied to the center of the acoustic reflector (1% agarose gel was used in this paper). Subsequently, the prepared hair phantom was rapidly attached to the acoustic reflector before the melted agarose solidified. This step was crucial to ensure the stability of the phantom during the detection process, preventing it from detaching. For the preparation of zebrafish larva, as depicted in Fig. 2(b), a zebrafish larva approximately 1.5 cm in length was placed in a meticulously fabricated cylindrical agarose gel mold. This mold featured a centrally concave groove for infusing water to facilitate the movement of the zebrafish. 1 or 2 drops of melted agarose were applied to the central surface of the acoustic reflector. The mold with the concave groove was then quickly attached to the acoustic reflector, and the zebrafish in water was covered. Over a few minutes, the melted agarose cooled and solidified. The agarose chamber filled with water minimized the movement of the zebrafish while ensuring its survival during the experiment. The preparation process of leaf skeleton phantom is similar to that of hair phantom, as depicted in Fig. 2(c). A black leaf skeleton is placed and embedded in agarose gel. This leaf skeleton phantom is then affixed to the central region of the acoustic reflector for experimental detection.

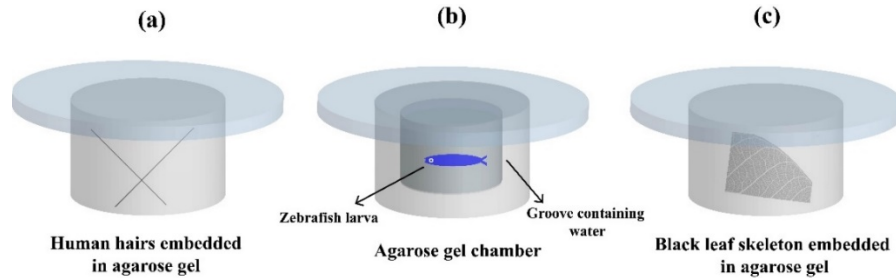


**Fig. 2.** Schematics of imaging samples inserted in agarose gels and attached to the acoustic reflector. (a) Two cross-tilted human hairs embedded in agarose gel. (b) A zebrafish larva placed in an agarose gel chamber. (c) A black leaf skeleton embedded in agarose gel.

## 2.3. Image reconstruction and processing

The 3D reconstruction of all PA images in this study was conducted utilizing the conventional delay-and-sum (DAS) algorithm [63,64]. Firstly, the PA image encompassing both non-reflected and reflected signals is reconstructed as a whole. The non-reflected signals correspond to ultrasonic waves captured directly by the detector array without the action of acoustic reflector. The reflected signals correspond to the ultrasonic waves that are reflected by the acoustic reflector and then received by the detector array. The non-reflected PA image and reflected PA image are spatially separated due to time delays of the ultrasonic waves received by the detector. The image reconstruction was executed on a cube with  $525 \times 525 \times 525$  voxels, and each voxel size was 0.067 mm. An iterative loop algorithm was employed to ascertain the optimal speed of sound during image reconstruction process. The speed of sound value was firstly set in a broad range, and then the optimal value was determined by evaluating image quality in the iterative reconstruction process (see Supplement 1).

To demonstrate the benefits of the acoustic reflector, we conduct a comparison of three image types, the non-reflected image, the reflected image, and the merged image that represents a superposition of both non-reflected and reflected images, respectively. During the image merging process, the non-reflected image and reflected image were reconstructed respectively.



Subsequently, the datasets of the two were aligned and added to form a composite image (see [Supplement 1](#), Fig. S2).

### 3. Experimental results

#### 3.1. Hair phantom imaging and system resolution measurement

To experimentally validate the proposed technique, we firstly imaged a phantom comprising two cross-placed human hairs. The phantom was irradiated by a pulsed laser with  $\lambda = 532$  nm. Figure 3(a) is the schematic related to the orientation of the hair phantom. Figures 3(b) and 3(c) display the reconstructed PA images of hairs in  $y-z$  and  $x-z$  planes, respectively. It should be noted that here we flipped the reflected image around the  $x-y$  plane to compare the results more intuitively. Each cross-sectional image represents a maximum amplitude projection (MAP). Comparing the non-reflected image and reflected image in Fig. 3(b) or Fig. 3(c), one can see that the hairs indicated by white arrows in the reflected image appear longer and finer than those observed in the corresponding areas of the non-reflected image. This phenomenon can be attributed to the effect of the acoustic reflector on ultrasonic waves, especially in regions located far from the acoustic reflector along the  $z$  direction. In the absence of an acoustic reflector, the obliquely downward-propagating ultrasonic waves generated by the hair are only captured by a limited number of detector elements. Meanwhile, the obliquely upward-propagating waves remain undetected. The presence of the acoustic reflector redirects these waves, allowing them to be received by a greater number of array elements due to the increased divergence angle (see [Supplement 1](#), Fig. S3). Consequently, the merged image superimposed by the non-reflected and reflected images, undoubtedly provides more sufficient and complete information than the non-reflected image.

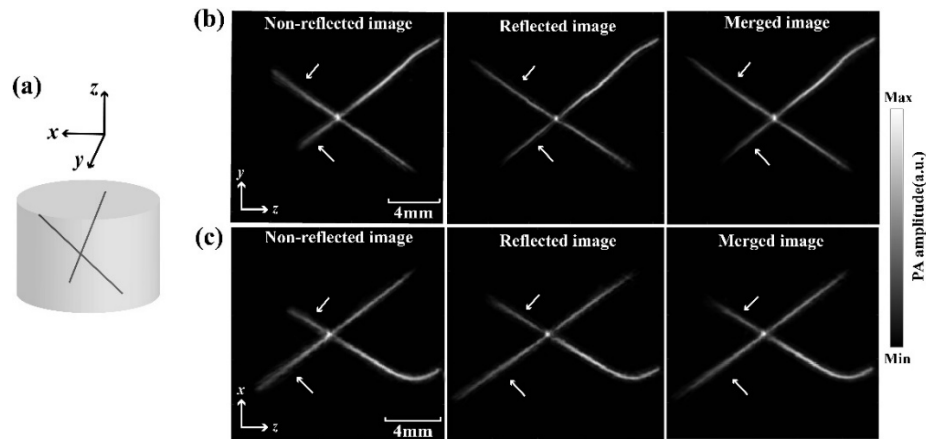


**Fig. 3.** Hair phantom images. (a) Schematic diagram of hair phantom. (b) Reconstructed PA images in  $y-z$  plane. (c) Reconstructed PA images in  $x-z$  plane. Each cross-sectional image is the MAP.

The spatial resolution of the system was evaluated by imaging a tungsten filament with a diameter of  $10\ \mu\text{m}$  embedded in gelatin phantom. The tungsten filament was aligned in horizontal plane, as shown in Fig. 4(a), and the 2D superposition images of tungsten filament in  $x-y$ ,  $y-z$  planes are displayed in Figs. 4(b) and 4(c), respectively. Figures 4(d) and 4(e) show the normalized PA amplitude distribution along the red dashed lines in Figs. 4(b) and 4(c), respectively. The lateral resolution, defined as the full width at half maximum (FWHM) of the amplitude distribution, is  $220\ \mu\text{m}$ . Similarly, the axial resolution is  $250\ \mu\text{m}$ . In addition, we present the spatial resolution of the non-reflective system, i.e., without the use of an acoustic

reflector, as depicted in Figs. 4(f) and 4(g). For the sake of brevity, the specific process is not be repeated. The non-reflective system achieves lateral and axial resolutions of  $224\ \mu\text{m}$  and  $282\ \mu\text{m}$ , respectively. By comparison, it can be seen that the incorporation of an acoustic reflector can enhance the resolution in  $z$  direction, which improves the spatial anisotropy.

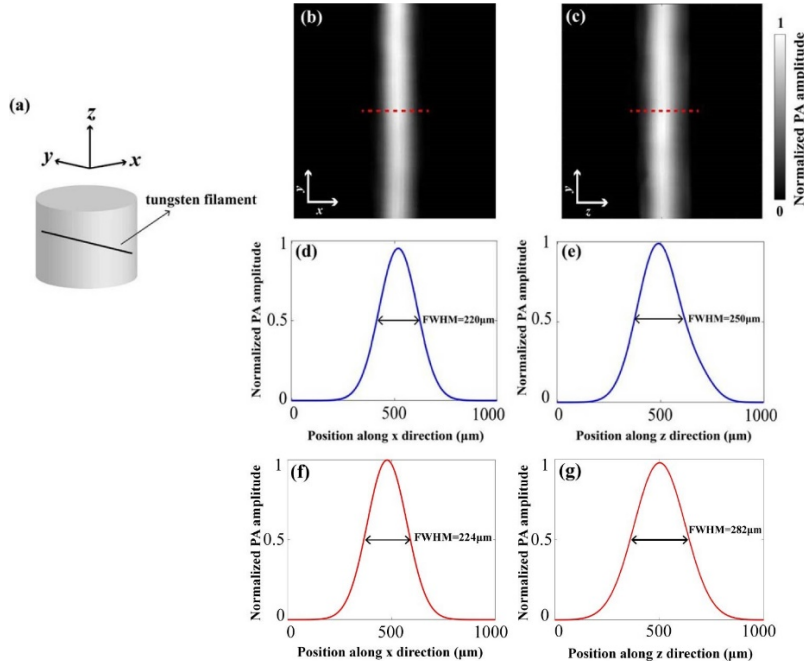


**Fig. 4.** Quantification of the spatial resolution of the 3D-PACT system based on the hemispheric array transducer combined with an acoustic reflector. (a) Schematic diagram of tungsten filament embedded in gelatin phantom. (b) (c) MAP images in  $x - y$ ,  $y - z$  planes of a tungsten filament with a diameter of  $10\ \mu\text{m}$  placed near the center of the detector. (d) (e) The normalized PA amplitude distribution along the red dashed lines in (b) and (c), corresponding the lateral and axial resolutions, respectively. (f) (g) The lateral and axial resolutions of non-reflected system, respectively.

### 3.2. In vivo zebrafish imaging

An in vivo zebrafish larva immersed within a gelatinous tank was prepared and imaged. Figure 5 presents the reconstructed PA images of the zebrafish at 800 nm light illumination. Figures 5(a) and 5(b) display MAPs in  $x - z$  and  $y - z$  planes, respectively. Each figure comprises both the non-reflected image (left) and reflected image (right). The orange dashed line in the figures indicates the position of the acoustic reflector surface. It reveals that the PA signals from certain tissues appear weak in the non-reflected image, whereas the reflected image exhibits more complete structural features, compensating for these deficiencies, particularly in the regions indicated by the white arrows. The generated ultrasonic waves propagating in the  $+z$  direction or oblique  $+z$  direction are undetectable without the acoustic reflector. Especially for the  $+z$  boundary parts near the surface of the sample, although some ultrasonic waves propagating along  $-z$  direction can be received by the detector array, there are two main points to be considered. On the one hand, the reception angle for these waves is smaller than that of the waves received after reflection by the acoustic reflector. On the other hand, the tissues underlying these boundary parts can cause sound attenuation. Therefore, in the reflected image, some PA waves that were originally undetected can be reflected by the acoustic reflector and received by a greater number

of detector elements. This results in richer information in certain areas, as indicated by the white arrows.

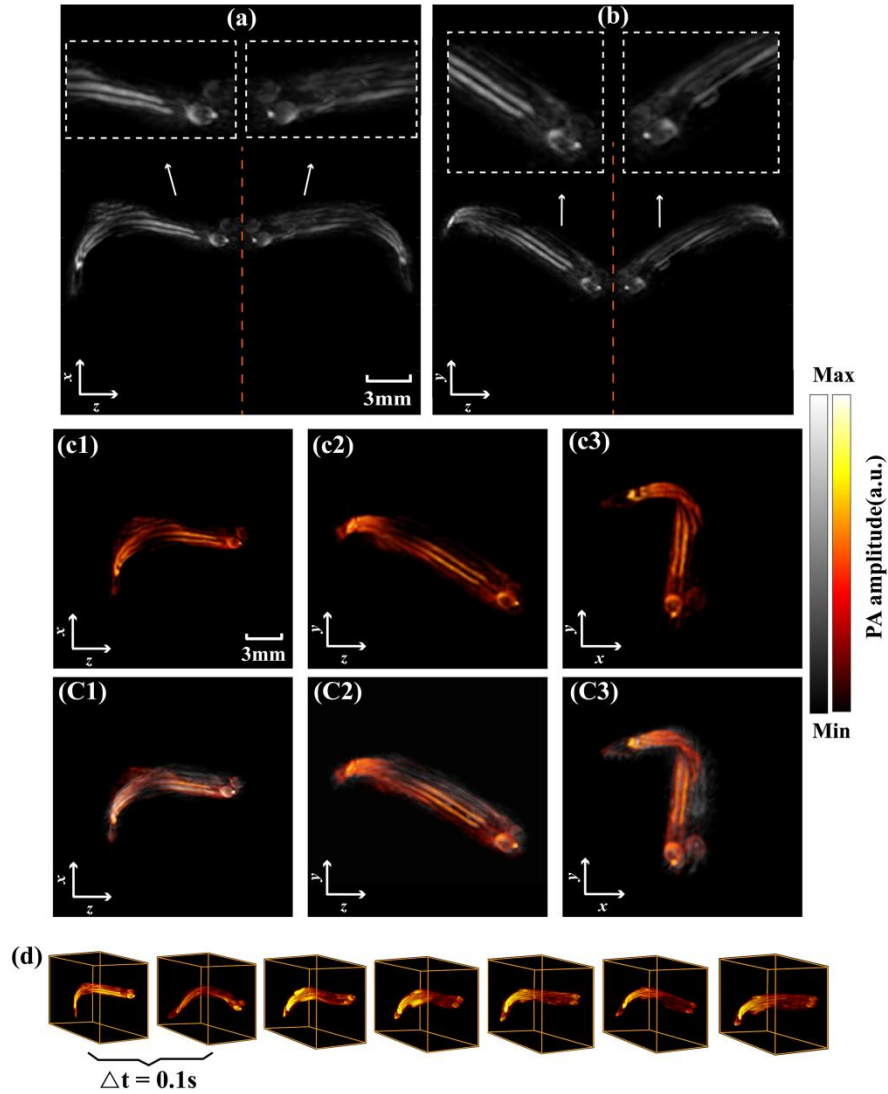


**Fig. 5.** In vivo PA images of a zebrafish larva. (a)(b) Cross-sectional images in  $x - z$  and  $y - z$  planes, respectively. The left sides in (a) and (b) represent images reconstructed from the non-reflected signals, and the right sides illustrate images reconstructed from reflected signals. The areas in the white dashed boxes are magnified versions of the corresponding images directly below them. (c1)–(c3) The cross-sectional images without reflected signals in  $x - z$ ,  $y - z$  and  $x - y$  planes, respectively. (C1)–(C3) The merged images, including both non-reflected and reflected signals, in  $x - z$ ,  $y - z$  and  $x - y$  planes, respectively. The hot color scale denotes non-reflected portion and the gray color scale denotes reflected portion. (d) 3D dynamic changes of the zebrafish within 0.7 s, and the interval between two adjacent frames is 0.1 s. Each cross-sectional image is the MAP.

For comparison, Figs. 5(c1)–5(c3) depict the reconstructed images in different cross sections of the non-reflected image, while Figs. 5(C1)–5(C3) present the merged patterns that combine both non-reflected and reflected images. The merged PA images provide a more complete



representation of the tissue structures, characterized by enhanced signal amplitude and improved image quality. To visualize the contrast between the two superimposed components, distinct color scales and a consistent threshold were applied to the images. A 3D multi-view display of the merged image for a zebrafish larva is presented in [Visualization 1](#). Moreover, we observed the real-time imaging of zebrafish movement. Figure 5(d) illustrates the dynamic changes of the zebrafish within 0.7 s, with each frame presented from the same perspective, and the interval between two adjacent frames is 0.1 s. An even more pronounced depiction of movement within 2 s timeframe is presented in [Visualization 2](#), which reveals the real-time dynamic imaging capability of the system.

### 3.3. Leaf skeleton phantom imaging

The effectiveness of the proposed method was also verified by imaging a leaf skeleton phantom. To evaluate the imaging capability of our system for the sample that deviate from the center of the detector array, a leaf skeleton phantom was positioned approximately 5 mm below the center of the detector array for PA imaging. The sample was irradiated by the pulsed laser with  $\lambda = 532$  nm. Figure 6 presents the structure maps from the same perspective, showing the non-reflected image and the merged image, respectively. The non-reflected image in Fig. 6(a), with only physical detector elements, reveals indistinct and intermittent vein structure. In contrast, the merged image in Fig. 6(b), consisting of both non-reflected and reflected images, displays more distinct and continuous veins that appear to be well differentiated. This result indicates that, to some extent, when certain regions of the imaging target deviate from the center of the detector, the presence of acoustic reflector can enhance the acquisition of information from these areas. This leads to an improvement in image quality and the overall integrity of the imaging results.

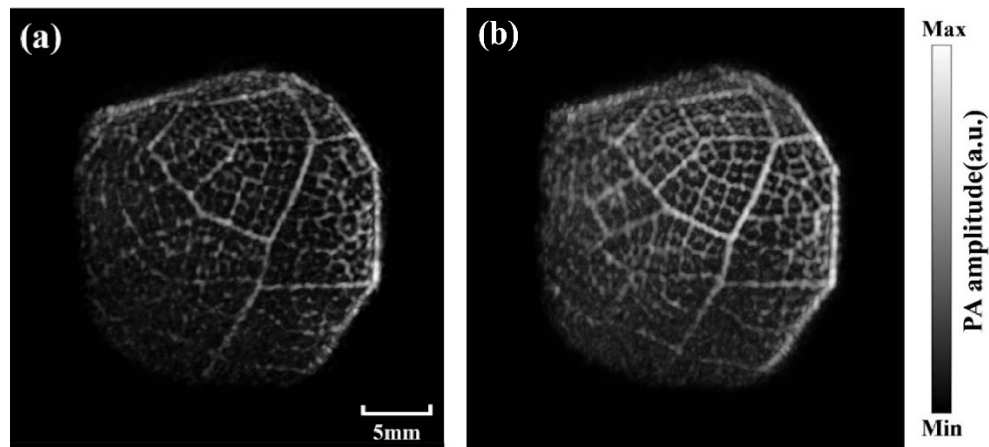


**Fig. 6.** Leaf skeleton phantom images. (a) The image reconstructed from the non-reflected signal. (b) The merged image including both non-reflected and reflected signals. Each cross-sectional image is the MAP.

## 4. Discussion

We have developed a PACT system that incorporates a hemispherical ultrasonic transducer array with a planar acoustic reflector to achieve a nearly enclosed, full-view detection range. The effectiveness of the proposed system was experimentally demonstrated by imaging distinct samples. We conducted a comparison of the non-reflected image, the reflected image, and the merged image that overlays the non-reflective and reflective images. By imaging a hair phantom,

it reveals that part of the ultrasonic signals, which are originally confined to a narrow reception angle, can be broadened through acoustic reflection. This allows for the reception of signals by an increased number of detection elements. Consequently, in certain area, the merged image exhibits superior resolution and encompasses more comprehensive image information compared to the non-reflected image. By imaging of an *in vivo* zebrafish larva, we demonstrated that the merged image is capable of recovering biological tissue information that was undetectable in the non-reflective image. Our results reveal that the system possesses a significant advantage in detecting and restoring obstructed or damaged ultrasonic signals, which can improve the overall diagnostic potential of the imaging modality. Moreover, we verified the dynamic imaging capability of the system. By imaging a leaf skeleton placed below the center of the detector array, the merged image exhibits more continuous and distinct vein details compared to the non-reflective image. This result indicates the imaging advantage, particularly for regions that are off-center from the detector.

The advantages of the proposed system are manifold. First, it eliminates the need for intricate mechanical rotation scanning or complex structural engineering. By employing a hemispherical transducer array combined with a glass-made acoustic reflector, the imaging speed is facilitated. Second, the method boasts exceptional imaging capabilities. It enables nearly full-view imaging of the sample, achieving an approximately  $3.7\pi$  solid angle coverage. If an acoustic reflector with a radius of 100 mm is employed, the detection view range can cover  $4\pi$  steradians. This results in isotropic spatial resolution, and the system demonstrated dynamic imaging capacity, allowing for the capture of real-time changes of the sample. Third, the image reconstruction is based on the DAS algorithm and the image synthesis relies on the alignment and superposition of the datasets, this as much as possible to reduce the time needed for data processing and computing resources. The system shows potential in clinical scenarios involving human subjects, but there are several challenges that require consideration: (1) Within the intricate environment of human tissues, the acoustic signal will pass through the tissue again during the reflection process. This may lead to signal loss and distortion, affecting the image quality. Image reconstruction algorithms need to be developed to compensate for signal attenuation and scattering, potentially integrating deep learning and adaptive subregional reconstruction algorithms to enhance data processing; (2) The integration of acoustic reflectors increases the complexity of the system, and it is necessary to design the device structure according to the detection location of the human body, such as movable brackets, which potentially increases the operating cost; (3) Based on acoustic reflector detection, high-resolution imaging requirements and data processing may result in longer acquisition and reconstruction times. This requires high-performance computers and optimized processing algorithms; (4) Although the PACT system offers a significant safety advantage over ionizing radiation methods, such as X-rays or CT scans, due to non-ionizing radiation, the need for deeper tissue penetration in the human body may demand higher laser power. Medical standards, safety and patient privacy issues need to be considered in practical applications.

## 5. Conclusion

In summary, we have developed a 3D-PACT system that combines an acoustic reflector with a hemispherical ultrasonic transducer array. A planar acoustic reflector was implemented as a mirrored virtual transducer array to effectively enlarge the detection view range to cover approximately  $3.7\pi$  steradians. This approach facilitates nearly an enclosed space for the object and full-view imaging. The feasibility of this system was validated by the imaging of a hair phantom, an *in vivo* zebrafish, and a leaf skeleton phantom. By superimposing the reflected signals with the non-reflected signal, we were able to visualize previously elusive tissue structures. The merged image exhibits enhanced signal strength and improved image quality compared to the non-reflected image. This system can offer advantages of a large field of view, isotropic spatial

resolution, fast imaging speed, and the capability for real-time dynamic imaging. These features render our 3D-PACT system a useful tool for further exploration in both preclinical research and clinical applications.

**Funding.** National Key Research and Development Program of China (2022YFC2808203).

**Disclosures.** The authors declare no conflicts of interest.

**Data availability.** Data underlying the results presented in this paper are not publicly available at this time but may be obtained from the authors upon reasonable request.

**Supplemental document.** See [Supplement 1](#) for supporting content.

## References

1. L. V. Wang and J. J. Yao, "A practical guide to photoacoustic tomography in the life sciences," *Nat. Methods* **13**(8), 627–638 (2016).
2. J. Yao, L. Wang, J. M. Yang, *et al.*, "High-speed label-free functional photoacoustic microscopy of mouse brain in action," *Nat. Methods* **12**(5), 407–410 (2015).
3. L. V. Wang and S. Hu, "Photoacoustic tomography: in vivo imaging from organelles to organs," *Science* **335**(6075), 1458–1462 (2012).
4. L. V. Wang, "Multiscale photoacoustic microscopy and computed tomography," *Nat. Photonics* **3**(9), 503–509 (2009).
5. P. Beard, "Biomedical photoacoustic imaging," *Interface Focus* **1**(4), 602–631 (2011).
6. L. Nie, Z. Guo, and L. V. Wang, "Photoacoustic tomography of monkey brain using virtual point ultrasonic transducers," *J. Biomed. Opt.* **16**(7), 076005 (2011).
7. J. Gamelin, A. Maurudis, A. Aguirre, *et al.*, "A real-time photoacoustic tomography system for small animals," *Opt. Express* **17**(13), 10489–10498 (2009).
8. D. Wang, Y. Wang, W. Wang, *et al.*, "Deep tissue photoacoustic computed tomography with a fast and compact laser system," *Biomed. Opt. Express* **8**(1), 112–123 (2017).
9. M. Jeon, J. Kim, and C. Kim, "Multiplane spectroscopic whole-body photoacoustic imaging of small animals in vivo," *Med. Biol. Eng. Comput.* **54**(2-3), 283–294 (2016).
10. H. P. Brecht, R. Su, M. Fronheiser, *et al.*, "Whole-body three-dimensional photoacoustic tomography system for small animals," *J. Biomed. Opt.* **14**(6), 064007 (2009).
11. L. Li, L. Zhu, C. Ma, *et al.*, "Single-impulse panoramic photoacoustic computed tomography of small-animal whole-body dynamics at high spatiotemporal resolution," *Nat. Biomed. Eng.* **1**(5), 0071 (2017).
12. M. L. Li, J. T. Oh, X. Xie, *et al.*, "Simultaneous molecular and hypoxia imaging of brain tumors in vivo using spectroscopic photoacoustic tomography," *Proc. IEEE* **96**(3), 481–489 (2008).
13. A. Oraevsky, R. Su, H. Nguyen, *et al.*, "Full-view 3D imaging system for functional and anatomical screening of the breast," *Proc. SPIE 10494, Photons Plus Ultrasound: Imaging and Sensing* (2018).
14. I. Kosik, M. Brackstone, A. Kornecki, *et al.*, "Intraoperative photoacoustic screening of breast cancer: a new perspective on malignancy visualization and surgical guidance," *J. Biomed. Opt.* **24**(5), 056002 (2019).
15. V. S. Dogra, B. K. Chinni, K. S. Valluru, *et al.*, "Multispectral photoacoustic imaging of prostate cancer: preliminary ex-vivo results," *J. Clin. Imaging Sci.* **3**, 4141 (2013).
16. R. A. Kruger, W. L. Kiser Jr, D. R. Reinecke, *et al.*, "Thermoacoustic computed tomography using a conventional linear transducer array," *Med. Phys.* **30**(5), 856–860 (2003).
17. L. Song, K. Maslov, K. K. Shung, *et al.*, "Ultrasoundarray-based real-time photoacoustic microscopy of human pulsatile dynamics in vivo," *J. Biomed. Opt.* **15**(2), 021303 (2010).
18. Y. Zeng, D. Xing, Y. Wang, *et al.*, "Photoacoustic and ultrasonic coimage with a linear transducer array," *Opt. Lett.* **29**(15), 1760–1762 (2004).
19. C. Kim, T. N. Erpelding, K. Maslov, *et al.*, "Handheld array-based photoacoustic probe for guiding needle biopsy of sentinel lymph nodes," *J. Biomed. Opt.* **15**(4), 046010 (2010).
20. C. Kim, T. N. Erpelding, L. Jankovic, *et al.*, "Performance benchmarks of an array-based hand-held photoacoustic probe adapted from a clinical ultrasound system for noninvasive sentinel lymph node imaging," *Philos. Trans. R. Soc., A* **369**(1955), 4644–4650 (2011).
21. A. Needles, A. Heinmiller, J. Sun, *et al.*, "Development and initial application of a fully integrated photoacoustic micro-ultrasound system," *IEEE Trans. Ultrason., Ferroelect., Freq. Contr.* **60**(5), 888–897 (2013).
22. D. Yang, D. Xing, S. Yang, *et al.*, "Fast full-view photoacoustic imaging by combined scanning with a linear transducer array," *Opt. Express* **15**(23), 15566–15575 (2007).
23. J. Gateau, M. A. Caballero, A. Dima, *et al.*, "Three-dimensional photoacoustic tomography using a conventional ultrasound linear detector array: whole-body tomographic system for small animals," *Med. Phys.* **40**(1), 013302 (2013).
24. J. Gateau, T. Chaigne, O. Katz, *et al.*, "Improving visibility in photoacoustic imaging using dynamic speckle illumination," *Opt. Lett.* **38**(23), 5188–5191 (2013).
25. W. Shu, M. Ai, T. Salcudean, *et al.*, "Broadening the detection view of 2D photoacoustic tomography using two linear array transducers," *Opt. Express* **24**(12), 12755–12768 (2016).

26. M. Schwarz, A. Buehler, V. Ntziachristos, *et al.*, "Isotropic high resolution optoacoustic imaging with linear detector arrays in bi-directional scanning," *J. Biophotonics* **8**(1-2), 60–70 (2015).
27. D. Wu, X. Wang, C. Tao, *et al.*, "Limited-view photoacoustic tomography utilizing backscatterers as virtual transducers," *Appl. Phys. Lett.* **99**(24), 2011–2014 (2011).
28. P. Burgholzer, C. Hofer, G. Paltauf, *et al.*, "Thermoacoustic tomography with integrating area and line detectors," *IEEE Trans. Ultrason., Ferroelect., Freq. Contr.* **52**(9), 1577–1583 (2005).
29. B. Huang, J. Xia, K. I. Maslov, *et al.*, "Improving limited-view photoacoustic tomography with an acoustic reflector," *J. Biomed. Opt.* **18**(11), 110505 (2013).
30. G. Li, J. Xia, K. Wang, *et al.*, "Tripling the detection view of high-frequency linear-array-based photoacoustic computed tomography by using two planar acoustic reflectors," *Quant. Imaging Med. Surg.* **5**(1), 57–62 (2015).
31. G. Li, J. Xia, K. I. Maslov, *et al.*, "Broadening the detection view of high-frequency linear-array-based photoacoustic computed tomography by using planar acoustic reflectors," *Proc. SPIE* **8943**, 89430H (2014).
32. R. Ellwood, E. Zhang, P. Beard, *et al.*, "Photoacoustic imaging using acoustic reflectors to enhance planar arrays," *J. Biomed. Opt.* **19**(12), 126012 (2014).
33. D. Razansky, A. Buehler, V. Ntziachristos, *et al.*, "Volumetric real-time multispectral optoacoustic tomography of biomarkers," *Nat. Protoc.* **6**(8), 1121–1129 (2011).
34. A. Buehler, E. Herzog, D. Razansky, *et al.*, "Video rate optoacoustic tomography of mouse kidney perfusion," *Opt. Lett.* **35**(14), 2475–2477 (2010).
35. G. Paltauf, P. Hartmair, G. Kovachev, *et al.*, "Piezoelectric line detector array for photoacoustic tomography," *Photoacoustics* **8**, 28–36 (2017).
36. J. Xia, M. R. Chatni, K. I. Maslov, *et al.*, "Whole-body ring-shaped confocal photoacoustic computed tomography of small animals in vivo," *J. Biomed. Opt.* **17**(5), 050506 (2012).
37. P. Wray, L. Lin, P. Hu, *et al.*, "Photoacoustic computed tomography of human extremities," *J. Biomed. Opt.* **24**(2), 026003 (2019).
38. M. Nasiravanaki, J. Xia, H. Wan, *et al.*, "High-resolution photoacoustic tomography of resting-state functional connectivity in the mouse brain," *Proc. Natl. Acad. Sci.* **111**(1), 21–26 (2014).
39. M. Heijblom, D. Piras, M. Brinkhuis, *et al.*, "Photoacoustic image patterns of breast carcinoma and comparisons with Magnetic Resonance Imaging and vascular stained histopathology," *Sci. Rep.* **5**(1), 11778 (2015).
40. X. L. Deán-Ben and D. Razansky, "Portable spherical array probe for volumetric real-time optoacoustic imaging at centimeter-scale depths," *Opt. Express* **21**(23), 28062–28071 (2013).
41. I. Ivankovic, E. Merčep, C. G. Schmedt, *et al.*, "Real-time volumetric assessment of the human carotid artery: handheld multispectral optoacoustic tomography," *Radiology* **291**(1), 45–50 (2019).
42. A. Taruttis, A. C. Timmermans, P. C. Wouters, *et al.*, "Optoacoustic imaging of human vasculature: feasibility by using a handheld probe," *Radiology* **281**(1), 256–263 (2016).
43. X. Luo, J. Jiang, H. Wu, *et al.*, "The influences of finite aperture size in photoacoustic computed tomography," *Ultrasonics* **133**, 107042 (2023).
44. R. Kruger, D. Reinecke, G. Kruger, *et al.*, "HYPR-spectral photoacoustic CT for preclinical imaging," *Proc. SPIE* **7177**, 71770F (2009).
45. R. B. Lam, R. A. Kruger, D. R. Reinecke, *et al.*, "Dynamic optical angiography of mouse anatomy using radial projections," *Proc. SPIE* **7564**, 756405 (2010).
46. R. A. Kruger, C. M. Kuzmiak, R. B. Lam, *et al.*, "Dedicated 3D photoacoustic breast imaging," *Med. Phys.* **40**(11), 113301 (2013).
47. M. Toi, Y. Asao, Y. Matsumoto, *et al.*, "Visualization of tumor-related blood vessels in human breast by photoacoustic imaging system with a hemispherical detector array," *Sci. Rep.* **7**(1), 41970 (2017).
48. L. Lin, P. Hu, J. Shi, *et al.*, "Single-breath-hold photoacoustic computed tomography of the breast," *Nat. Commun.* **9**(1), 2352 (2018).
49. L. Lin, P. Hu, X. Tong, *et al.*, "High-speed three-dimensional photoacoustic computed tomography for preclinical research and clinical translation," *Nat. Commun.* **12**(1), 882 (2021).
50. S. Choi, J. Yang, S. Y. Lee, *et al.*, "Deep learning enhances multiparametric dynamic volumetric photoacoustic computed tomography in vivo (DL-PACT)," *Adv. Sci.* **10**(1), 2202089 (2023).
51. L. C. M. Yip, P. Omid, E. Rascevska, *et al.*, "Approaching closed spherical, full-view detection for photoacoustic tomography," *J. Biomed. Opt.* **27**(8), 086004 (2022).
52. C. Zhang and Y. Wang, "Deconvolution reconstruction of full-view and limited-view photoacoustic tomography: a simulation study," *J. Opt. Soc. Am. A* **25**(10), 2436–2443 (2008).
53. J. Meng, C. Liu, J. Kim, *et al.*, "Compressed sensing with a Gaussian scale mixture model for limited view photoacoustic computed tomography in vivo," *Technol. Cancer Res. Treat.* **17**, 1533033818808222 (2018).
54. X. Liu, D. Peng, X. Ma, *et al.*, "Limited-view photoacoustic imaging based on an iterative adaptive weighted filtered backprojection approach," *Appl. Opt.* **52**(15), 3477–3483 (2013).
55. C. Tao and X. Liu, "Reconstruction of high quality photoacoustic tomography with a limited-view scanning," *Opt. Express* **18**(3), 2760–2766 (2010).
56. P. Omid, M. Zafar, M. Mozaffarzadeh, *et al.*, "A novel dictionary-based image reconstruction for photoacoustic computed tomography," *Appl. Sci.* **8**(9), 1570 (2018).

57. D. M. Egolf, R. K. W. Chee, R. J. Zemp, *et al.*, “Sparsity-based reconstruction for super-resolved limited-view photoacoustic computed tomography deep in a scattering medium,” *Opt. Lett.* **43**(10), 2221–2224 (2018).
58. H. Yang, D. Jüstel, J. Prakash, *et al.*, “Soft ultrasound priors in photoacoustic reconstruction: Improving clinical vascular imaging,” *Photoacoustics* **19**, 100172 (2020).
59. A. Hauptmann, F. Lucka, M. Betcke, *et al.*, “Model-based learning for accelerated, limited-view 3-D photoacoustic tomography,” *IEEE Trans. Med. Imaging* **37**(6), 1382–1393 (2018).
60. H. Zhang, H. Li, N. Nyayapathi, *et al.*, “A new deep learning network for mitigating limited-view and under-sampling artifacts in ring-shaped photoacoustic tomography,” *Comput. Med. Imaging Graphics* **84**, 101720 (2020).
61. M. W. Kim, G. S. Jeng, I. Pelivanov, *et al.*, “Deep-learning image reconstruction for real-time photoacoustic system,” *IEEE Trans. Med. Imaging* **39**(11), 3379–3390 (2020).
62. T. Tong, W. Huang, K. Wang, *et al.*, “Domain transform network for photoacoustic tomography from limited-view and sparsely sampled data,” *Photoacoustics* **19**, 100190 (2020).
63. S. K. Kalva and M. Pramanik, “Experimental validation of tangential resolution improvement in photoacoustic tomography using modified delay-and-sum reconstruction algorithm,” *J. Biomed. Opt.* **21**(8), 086011 (2016).
64. S. Hakakzadeh, M. Amjadian, Y. Zhang, *et al.*, “Signal restoration algorithm for photoacoustic imaging systems,” *Biomed. Opt. Express* **14**(2), 651–666 (2023).